Unveiling the role of copper content in the crystal structure and phase stability of epitaxial Cu(In,Ga)S2 films on GaP/Si(001)

Eugène Bertin, Olivier Durand, Antoine Létoublon, Charles Cornet, Ludovic Arzel, Leo Choubrac, Rozenn Bernard, Éric Gautron, Sylvie Harel, Maud Jullien, et al.

Unveiling the Role of Copper Content in the Crystal Structure and Phase Stability of epitaxial $Cu(In,Ga)S_2$ Films on GaP/Si(001)

Eugène Bertin[a,b,*], Olivier Durand[a], Antoine Létoublon[a], Charles Cornet[a], Ludovic Arzel[b], Leo Choubrac[b], Rozenn Bernard[a], Éric Gautron[b], Sylvie Harel[b], Maud Jullien[a], Tony Rohel[a], Lionel Assmann[b], Nicolas Barreau[b]

[a] *Univ Rennes, INSA Rennes, CNRS, Institut FOTON - UMR 6082, F-35000 Rennes, France*

[b] *Nantes Université, CNRS, Institut des Matériaux Jean Rouxel – UMR6502, F-44000 Nantes, France.*

* *Corresponding author*

1 Abstract

This study examines the growth condition to obtain a single-phase $Cu(In,Ga)S_2$ (CIGS) chalcopyrite film epitaxially grown by coevaporation on a GaP/Si(001) pseudo-substrate. In particular, we report the structural differences between KCN-etched Cu-rich and Cu-poor $Cu(In,Ga)S_2$ (CIGS) films coevaporated on GaP/Si(001) by 1-stage process. The Cu-poor CIGS film consists of at least three phases; the main crystal is found to be chalcopyrite-ordered, coexisting with In-rich $CuIn_5S_8$, and CuAu-ordered $CuInS_2$, all sharing epitaxial relationships with each other and the GaP/Si(001) pseudo-substrate. On the other hand, the Cu-rich CIGS film is single-phase chalcopyrite and displays sharper X-ray diffraction peaks and a lower density of microtwin defects. The elimination of the secondary CuAu-ordered phase with Cu excess is demonstrated. In both films, the chalcopyrite crystal exclusively grows with its c-axis aligned with the out-of-plane direction of Si[001]. This study confirms prior findings on the thermodynamics of Cu-In-Ga-S and the stability of secondary phases.

2 Keywords

- Phase stability
- Wide bandgap CIGS
- Epitaxial growth
- GaP/Si(001)
- Tandem solar cells
- X-ray diffraction

3 Introduction

In the family of $Cu(In,Ga)(S,Se)_2$ (CIGSSe) compounds, pure-sulfide $Cu(In,Ga)S_2$ (CIGS) attracts much attention in the photovoltaic community as its bandgap may be tuned from 1.54 eV, for $CuInS_2$ (CIS), to 2.43 eV, for $CuGaS_2$ (CGS) [1], making it suitable both for single-junction as well as tandem solar cells. Indeed, a practical route towards low-cost high efficiency solar cells is the integration of CIGS on crystalline Si (c-Si) in a 2 terminal monolithic configuration [2–4]. In a tandem cell context, the $CuIn_{0.75}Ga_{0.25}S_2$ chalcopyrite displays a near ideal bandgap of 1.7eV for a top cell absorber. This has renewed interest for CIGS, leading to reported efficiencies over 15% for CdS/CIGS [5] and Zn(O,S)/CIGS [6] heterojunction solar

cell grown by coevaporation on Mo-coated soda lime glass (SLG) substrate. To translate such advances to Si-based tandem cells, one first needs to replace the opaque Mo/SLG substrate by a Si substrate. The integration of 1.7eV CIGS on Si poses many challenges, such as possible out-diffusion of Cu into Si [7] and non-existent optimal interconnect between wide band-gap CIGSSe and Si [8].

Furthermore, it has been postulated several times that extended defects like grain boundaries might be detrimental for such wide bandgap (>1.6eV) CIGSSe semiconductors [9,10]. Comparatively to CIGS sulfides, much more is known on Se-based $Cu(In,Ga)Se_2$ (CIGSe). As of yet, polycrystalline CIGSe photovoltaic solar cells hold the record efficiency of 22.6% [11] for a Ga to group III ratio, GGI = [Ga]/([In]+[Ga]), of about 0.3. In CIGSe with low Ga content, grain boundaries (GBs) are reported to be electrically benign [12]. However, for GGI > 0.4, Cu-enriched GBs may become electrically active defects providing shunt paths [9], partially explaining the relatively low efficiency of wide band gap Ga-rich CIGSe films [13]. Epi-CIGSe displays a record efficiency of 20.0% [14,15] for a higher graded GGI of 0.4 (front) to 0.7 (rear); relatively high efficiency for such a high Ga content which may be explained by the absence of GBs. In contrast, very little is known on GBs in Ga containing CIGS sulphides [10]. We speculate that reducing the number of random angle GBs defects in wide bandgap 1.7eV CIGS constitutes a pathway towards higher efficiency. One method to prevent the formation of GBs is to grow epitaxial films onto monocrystalline substrate. This motivates the growth of epi-CIGS.

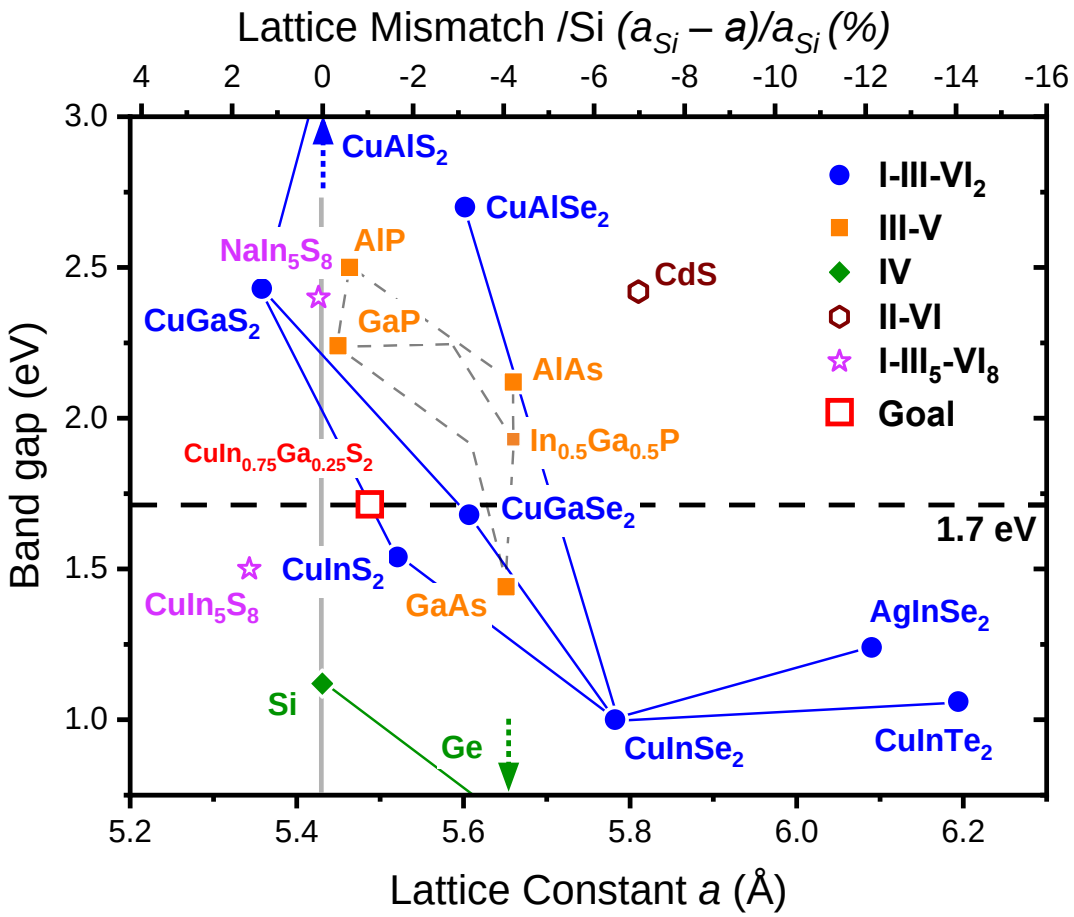

Figure 1: Band gap vs. lattice mismatch for chalcopyrites, silicon and III-V [16]. Gallium phosphide GaP is quasi lattice matched with Si. Additionally, in the Cu(In,Ga)(S,Se)$_2$ family, $CuIn_{0.75}Ga_{0.25}S_2$ sulfides have near ideal band gap for top cell applications. Lattice mismatch relative to a_{si} the lattice constant of Si is represented on the top x-axis scale.

Several successes around the epitaxial integration of CIGS on III-V or group IV (Si, Ge) substrates are reported. Si substrates are often used to minimize the system's lattice mismatch ($|f_{Si}^{CIGS}| < 1.6\%$), leading to several successful epitaxial growth of CIGS on (001)-oriented [17–20] as well as (111)-oriented [21,22] Si wafers. A 3.2 % efficient CdS/epi-CIS/Si(p) cell is demonstrated by Hahn et al. in 2005 [22]. It is worth mentioning reports of epitaxial CGS [23,24] and CIS [25,26] on (001)-oriented GaP wafers. Furthermore, the possibility of the epitaxial growth of CGS and CIS on III-V GaAs [17] and CaF_2 [27] cubic substrates respectively was explored successfully. With the exception of ref. [20], epitaxy achievements on Si wafers have been obtained by molecular beam epitaxy or metalorganic vapour-phase epitaxy. In contrast, in CIGS production lines, the industrially relevant processes are coevaporation and sulfurization of metallic precursors. In both process, CIGS adhesion on Si can be problematic [28].

In this article, we expose our method to alleviate some of the latter challenges, by evaporating CIGS on GaP/Si(001) pseudo-substrate. In GaP/Si(001), the GaP is quasi-lattice-matched with the Si substrate, with a lattice mismatch of 0.37% at room temperature [29]. The motivation for the introduction of a thin GaP interlayer between the CIGS and the Si is

threefold. Firstly, the high affinity of GaP for S [30] should favour the epitaxy of CIGS on GaP/Si(001), which would promote the fabrication of a high quality, dense and adherent CIGS film, with a minimal density of GBs. Indeed, as shown in Figure 1, a 1.7eV bandgap $CuIn_{0.75}Ga_{0.25}S_2$ film shares crucial similarities with GaP and Si in terms of lattice parameters (lattice mismatch $|f| < 1.6\%$ with GaP and Si) and crystal structure. The $CuIn_{0.75}Ga_{0.25}S_2$ chalcopyrite is a pseudo-cubic crystal whose structure is derived from the zinc-blend and the diamond structures of GaP and Si, respectively. Secondly, the GaP epitaxial layer should impede the diffusion of potentially harmful species like Cu from the CIGS to the Si. Thirdly, GaP, known for its low absorption coefficient [31], has a 2.26eV indirect bandgap [32] and an electron affinity of 3.8eV. GaP valence band should therefore be aligned with that of CIGS assuming an electron affinity of 4.7eV [33,34] for the latter. Additionally, GaP's conduction band should uplift a potential barrier for electrons. This theoretically makes GaP an ideal CIGS passivating selective contact for holes. More details can be found in a recent article where we exposed our motivation for growing $CuGaSe_2$ on GaP/Si(001) [35].

One of the main challenges for the growth of quality epitaxial CIGS is the complexity of Cu-In-Ga-S chemical system [36,37]. Indeed, in addition to the desired chalcopyrite (CH) CIGS phase, several secondary phases like the notorious thiospinel (TS) $CuIn_5S_8$ and $Cu_{2-x}S$, as well as the CuAu-ordered (CA) CIS and zinc-blend (ZB) CIS are reported [37] – Nota bene: these acronyms will be often used throughout this article-.

In the case of epi-CIGS grown by molecular beam epitaxy on Si [21,38], one can find systematic studies on the influence of the Ga content, or GGI, on the film's structural properties. Interestingly, they conclude to the coexistence of ZB, CA alongside the CH for In-rich CIGS (GGI < 0.4), including the relevant 1.7eV $CuIn_{0.75}Ga_{0.25}S_2$. Otherwise, Ga-rich CIGS (GGI > 0.4) crystallize as single-phase CH. On the other hand, studies on polycrystals and powder conclude that the most important parameter determining the stability of secondary phases is the Cu content of the film. However, to the best of our knowledge, no study aimed at understanding the influence of the overall Cu content on the structural properties on epi-CIGS. In this article, we aspire to fill the latter gap by investigating the crystallographic properties of samples grown in either Cu-deficient or Cu-excess conditions, relative to the 1:1:2 stoichiometry of CIGS.

In the following, we compare two $Cu(In,Ga)S_2$ films deposited by 1-stage coevaporation on GaP/Si(001) at 570°C. The first CIGS sample, labelled Cu-poor, is coevaporated in Cu-deficient conditions. A second CIGS sample, labelled Cu-rich, is coevaporated in Cu-excess conditions, and subsequently etched in KCN to remove any $Cu_{2-x}S$ residue from the surface. Firstly, we present the different candidate phases in the Cu-In-Ga-S system for clarity. Then, we thoroughly investigate by X-ray diffraction and Raman spectroscopy the structural properties of the main CH phase, in order to study its epitaxial relationship with the GaP/Si(001) pseudo-substrate. Then, we confront the Cu-poor to the Cu-rich samples, by comparing the presence of secondary phases in the two samples. Finally, we discuss the stabilisation of the CuAu-ordered secondary phase with Cu-deficiency.

4 Materials and methods

4.1 Epitaxial growth of GaP on Si(001) substrates

Prior to GaP epitaxy, the p-type Si(001) substrate with a 6° offset towards [110] (ref. [39]) is deoxidized ex-situ with a sequential HF(5%)/UV-O_3/HF(5%) treatment, followed by an in-situ vacuum annealing at 800°C. A 30nm-thin pseudomorphic GaP layer is epitaxially grown on Si at 500°C using a solid-source Molecular Beam Epitaxy (MBE) reactor [40], at the V/III ratio of 2. The GaP thickness is below the critical thickness of 45 to 95nm [29], which prevents the formation of relaxation dislocations. Therefore, the in-plane lattice parameter of the strained GaP film is that of Si.

4.2 Coevaporation of Cu(In,Ga)S_2

Prior to Cu(In,Ga)S_2 growth, GaP/Si(001) pseudo-substrates are deoxidized ex-situ in HCl(3.7%) solution for 1min. GaP/Si platforms are then quickly placed in vacuum on a pyrolytic carbon sample holder. The Cu(In,Ga)S_2 films are deposited on GaP/Si(001) by thermal co-evaporation from elemental sources of Cu (99.999%), Ga (99.9999%), In (99.999%) and S (99.99%) in a dedicated high vacuum chamber (base pressure 10^{-5} mbar). The substrates are heated with IR-lamps. During the 45min substrate temperature ramp up to the deposition temperature, the GaP/Si is exposed to the S flux. During the deposition process, the substrates are maintained at a temperature of 570°C, as measured with a thermocouple positioned on the backside of the substrates. We set the S flux to about 10 to 20 times the combined metal fluxes; such S excess prevents the formation of detrimental intermetallic phase clusters.

Two CIGS runs are performed on the same GaP/Si(001) platform. Although the acronym CIGS implies the 1:1:2 stoichiometry of Cu(In,Ga)S_2, we shall use the term Cu-poor and Cu-rich CIGS to refer to quaternary any Cu-In-Ga-S film grown in Cu-deficient or Cu-excess conditions. The Cu-poor sample is grown at a rate of 17 nm/min in Cu-deficient conditions and investigated as grown. The Cu-rich sample is grown at a rate of 22 nm/min in Cu-excess conditions, and subsequently undergoes a 2min KCN etching process in aqueous solution to remove $Cu_{2-x}S$ clusters from the surface.

4.3 X-ray diffraction experiments

X-ray diffraction (XRD) measurements are performed with a 5-circle Rigaku SmartLab diffractometer equipped with a HyPix-3000 2D X-ray detector. High-resolution scans are obtained with 2.5° Soller slit as receiving optics and a 2-bounce Ge(220) monochromator as incident optic in order to reduce the beam divergence and select the Cu $K\alpha_1$ radiation with a wavelength of 0.15406 nm. Low-resolution scans are obtained with 2.5° Soller slits as incident and receiving optics, coupled with a Ni Cu-kβ filter. Longitudinal ω/2θ scans are corrected to the theoretical position of the Si(004) Bragg peak. Peaks in low resolution scans are fitted with a sum of two pseudo-Voigt corresponding to the $K\alpha_1$ and $K\alpha_2$, with constrained areas and positions. Theoretical 2θ positions are calculated with VESTA [41] from lattice parameters of ref. [36,42] for CuAu-ordered CIS and $CuIn_5S_8$ respectively, and

ref. [36] for CIGS chalcopyrite. For the latter, theoretical positions are given for $CuIn_{0.8}Ga_{0.2}S_2$.

Pole figures are measured in low resolution mode without Ni Cu-kβ filter. Indexation of reflections on the pole figures has been performed with the help of STEREOPOLE software [43], which allows to superimpose the experimental pole figure data and the stereographic projection of candidate crystals. The $\varphi = 0°$ azimuth corresponds to the Si[110] direction of the miscut's descending steps.

4.4 Raman spectroscopy

Raman spectra are collected on absorbers with a Renishaw inVia micro-Raman system, using a λ=514nm laser as an excitation source. Raman spectra are fitted with Lorentzian peaks. Assuming a spot size of 1.5λ in diameter, the incident power density is calculated to be 25 kW/cm^2. For an excitation at 514nm and assuming an extinction coefficient of k = 0.5 [44], the penetration depth, i.e. the probed thickness, is calculated to be $\delta_p = \lambda/4\pi k = 82nm$, meaning only the first 100nm of CIGS from the surface are analysed. Peaks are fitted using Lorentzian functions and are drawn as a guide for the eye. Each peak does not necessarily correspond to a specific or unique phonon mode.

4.5 Energy dispersive spectroscopy

The chemical compositions of the films are determined by using Energy-dispersive X-ray spectroscopy (EDX) at 20kV acceleration voltage with a JEOL JSM 5800LV electron microscope equipped with an EDX SAMx detector. Quantification results are available in supplementary information Table S1. In $CuIn_{0.75}Ga_{0.25}S_2$/GaP(30nm)/Si stacks, 10 000 electron trajectories and 10 000 X-rays generation events were calculated with Casino software [45] at 20kV acceleration voltage. The density of $CuIn_{0.75}Ga_{0.25}S_2$ is calculated from ref. [46,47] and GaP and Si density is taken from ref. [48,49]. Results

5 Results

5.1 Thermodynamics of the Cu-In-Ga-S system

This article deals with epitaxial thin films; therefore, to analyse the data, *ab initio* refinement or comparison with powder diffraction patterns database is not possible. Consequently, to interpret the data, it is important to have a coherent picture of the candidate phases in the Cu-In-Ga-S. In the following, we review and comment the thermodynamic stability of the possible phases in the latter chemical system.

One of the many challenges of pure-sulfide CIGS is its notoriously complex chemistry, which unfolds when the film's Cu content, defined as the CGI=[Cu]/([In]+[Ga]), differs from the ideal $Cu(In,Ga)S_2$ stoichiometry [36,50]. On the Cu-rich side (CGI > 1), the excess in Cu atoms is accommodated by the formation of $Cu_{2-x}S$ alongside the CH phase [37]. On the Cu-poor side (CGI < 1) i.e. when the film is grown in copper deficient conditions, excess III atoms (In and Ga) are accommodated by the segregation of a variety of competing parasitic phases, the most common being the $CuIn_5S_8$ thiospinel phase.

A very comprehensive study of the entire pool of known candidates, including the metastable competitors, has been published by Larsen et al. [37], demonstrating the considerable complexity of the Na-Cu-In-Ga-S system. For simplicity's sake, we represent the relevant candidates, and their associated acronym, in Table 1, ruling out the Na-containing compounds. The stoichiometric (CGI=1) CIGS compound crystallizes in the chalcopyrite (CH) tetragonal system, which can be visualized as a stack of two cubic zinc-blend lattices. Its original cationic sublattice ordering is apparent in the <100> zone-axis, in which we can clearly see that Cu and group III atoms are organized in doublets orientated in the c-axis direction. The CH is known to easily alloy In and Ga. In Cu-poor CIGS (CGI <1), studies of polycrystalline films or powders reveal additional candidates that coexist with the CH. Firstly, in CuAu-ordered (CA) CIS compounds, the cations are organised in the form of planes composed of Cu or In exclusively, stacked in the [001] direction. While CA and CH crystal structures are very similar, their electronic properties differ since the CA is reported to exhibit a metallic behaviour [42]. Secondly, the n-type $CuIn_5S_8$ Cu-poor/In-rich phase was found to adopt a thiospinel (TS) structure [36,51]. Lastly, the zinc-blend (ZB) CIS phase (space group $F\bar{4}3m$) is characterised by a complete disorder of the cationic sublattice (see ref [37] for more details). One should note that the four structures have similar lattice parameters and symmetries; therefore, one can expect that the coexisting crystals can share epitaxial relationships.

Table 1: Description of the different phases of the Cu-In-Ga-S system relevant for this work. The crystals are represented with Vesta [41] in directions corresponding to the <100> zone-axis of the CH phase, rather than in directions corresponding to each crystal symmetry, to emphasize the crystallographic similarities (Blue: copper, Pink: III atoms, Yellow: sulfur). Note that the orientation of the sketches are chosen to match the orientation relation between the different phases determined in this work.

	Chalcopyrite (CH)[36]	**CuAu-ordering (CA)**[42]	**Thiospinel (TS)**[36]	**Zinc-blende (ZB)**[42]
<100>$_{CH}$ Vesta sketch	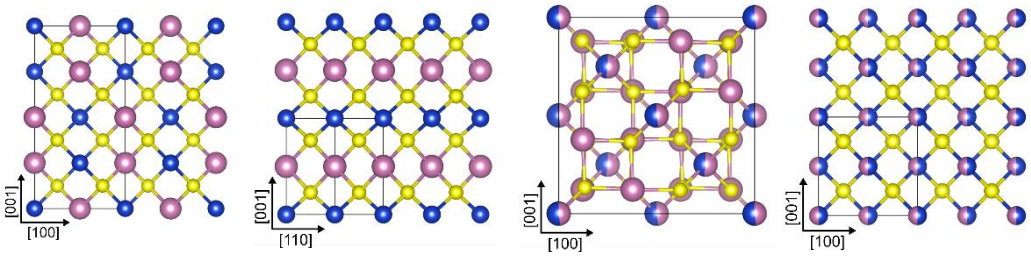			
Compo.	$Cu(In,Ga)S_2$	$CuInS_2$	$CuIn_5S_8$	$CuInS_2$
Space group	$I\bar{4}2d$	$P\bar{4}m2$	$F\bar{4}3m$	$F\bar{4}3m$
Lattice parameter (Å)	For GGI = 0.2: a = 5.49 c = 11.00	$\sqrt{2}$a = 5.56 2c = 10.98	a = 10.69	a = 5.52
Comment	Required phase	Metallic behaviour	Detrimental, n-type	Cationic disorder

5.2 Determination of films composition

Before going further, we assess the composition of the Cu-poor and KCN-etched Cu-rich samples by EDX (see Table S1 for detailed quantifications results). The 850nm-thick Cu-poor film exhibits a CGI=0.70 and a GGI=0.16, while the 1.1µm-thick Cu-rich sample after KCN etching has a CGI=0.93 and a GGI=0.14. Raman spectroscopy has been used to verify that $Cu_{2-x}S$ were indeed removed from the Cu-rich sample surface. On Figure 2(d), the peak associated with the A_1 mode of $Cu_{2-x}S$ disappeared after KCN etching, demonstrating that no $Cu_{2-x}S$ is present on the surface after the chemical treatment.

A CGI different from unity for the KCN-etched Cu-rich is unexpected since, from a thermodynamic standpoint, one would expect the as-grown Cu-rich to be composed of a mixture of stoichiometric CH and $Cu_{2-x}S$. We interpret this discrepancy as follows: assuming that P from the GaP does not incorporate into the CIGS in quantities above the EDX detection threshold, the fact that about 1% P is unambiguously detected suggested some 2.0keV P Kα photons escape from the GaP interlayer through the CIGS film. It is therefore also expected that some collected 9.2keV Ga Kα photons also originate from the GaP layer. We can thus infer that the Ga content of CIGS film is overestimated and that the CGI is underestimated, for both the Cu-rich and the Cu-poor sample. To verify this assumption, Casino simulations [45] have been performed. In the case of a 20keV electron beam striking 850nm and 1.1µm $CuIn_{0.75}Ga_{0.25}S_2$ films on GaP(30nm)/Si (see Figure S1), most Ga Kα X-ray

photons generated in GaP are able to escape the sample and be collected as displayed in Figure S2. To a lesser extent, the same holds for P Kα photons, which escape through the CIGS layer with a lower probability than Ga Kα photons. This shows that the precise determination of the composition of our samples is not trivial.

We define the chalcogen-to-metals ratio as SCGI=[S]/([Cu]+[In]+[Ga]). We measure a SCGI of 1.13 and 1.07 for the Cu-poor and the KCN-etched Cu-rich samples respectively. The slightly larger SCGI of the Cu-poor sample may be related to the anticipated presence of TS-$CuIn_5S_8$, which intrinsically has a SCGI=1.33 above unity. For the Cu-rich sample, we argue a SCGI different from unity may be related to the complex geometry of the stacks, which introduces quantification errors. In summary, EDX data is compatible with the 1:1:2 of CH-CIGS, although we cannot exclude that the films are marginally S-rich.

5.3 Demonstration of epitaxial CH-Cu(In,Ga)S_2 on GaP/Si(001)

In this subsection, we put a strong focus on the main phase, and determine its orientation relative to the GaP/Si(001) substrate. Since several cubic and tetragonal indexation system, will be used throughout this article, we start by clarifying one thing. In the tetragonal CH system, the d-spacing of (200) and (020) planes approximately correspond to that of (004) planes. On the contrary, in the ZB cubic system, the (200), (020) and (002) planes are equivalent. In order to prevent potential confusion, we will indicate when needed the use of the tetragonal chalcopyrite system with the subscripts CH. For example, the (111) planes correspond to the $(112)_{CH}$ planes. For non-CH phases, the Miller indices will be given with the conventional index system of the relevant phase and with the CH index system.

Figure 2(a) shows a low resolution ω/2θ scan along the Si[001] for the Cu-poor and the Cu-rich sample, obtained in experimental conditions favouring intensity over angular resolution, in order to evidence phases with low diffracting volume. Apart from the contributions of the GaP/Si(001) pseudo-substrate, one can note on Figure 2(a) two intense reflections marked with the symbol ∏ at about 2θ = 32.5° and 68.2° for both samples. In the Cu-poor sample exclusively, additional weak reflections marked with Ξ at 2θ = 16.1° and 50.0°, and moderately intense contributions labelled ‡ at 33.8° and 71.2° can be seen. In the following, each contribution will be clarified independently, starting with the strongest contributions.

In Figure 2(a), the most intense reflections ∏ at 2θ of 32.5° and 68.2° can be indexed either as $(h00)_{CH}$ or $(00\lambda)_{CH}$ planes of the CH system for both samples. To demonstrate that, a Raman spectrum has been recorded for the Cu-rich sample, for which only the most intense reflections at 2θ of 33° and 68° are observed in XRD. The spectrum of the Cu-rich sample is presented in Figure 2(d), and is characterised by a sharp and intense peak at 293cm^{-1}, alongside weak satellite peaks. We recall that, for such high absorption materials, only the first 100nm are probed (see Materials and methods). The Raman spectra of the Cu-rich sample is characteristic of Cu-rich CH [37,52], demonstrating that the Cu-rich surface crystallizes as a CH. In principle, the Raman does not rule out the presence of non-CH crystals deeper into the CIGS films. However, several studies have shown that In-rich/Cu-poor secondary phases tend to segregate at the surface [53] in the case of polycrystalline films. Therefore, Raman spectroscopy applied to the Cu-rich demonstrate that the strongest

reflections of Figure 2(a) can be ascribed to the CH, for both samples. The Raman and XRD data is perfectly compatible with the Cu-rich sample being single-phase CH.

There are several possible configurations to accommodate the tetragonal CIGS CH lattice on a (001)-orientated cubic crystal [18]. The tetragonal lattice may (i) sit upwards, with its c-axis orthogonal to the substrate surface ("c-growth" variant) or (ii) lie horizontally, with its c-axis contained in the substrate's surface plane, allowing two additional "a-growth" variants. In the literature, films where a-growth and c-growth variants coexist are demonstrated on both Si [18] and GaAs [17] with a prevalence of the c-growth variants. To elucidate the growth direction of the CH phase in our samples, we perform pole figure measurements at the Bragg angle of the CH(013) reflections, for both samples, as displayed Figure 2(b)(c). The Si(001) reference planes are offset from the center of the pole figures towards the $\varphi = 180°$ azimuth, by a tilt of $\chi = 6°$ [54], due to the sample miscut. In Figure 2(b)(c), four strong reflections can be found in the <110> azimuths while 4 weaker reflections are found in the <100> azimuths. CH(112) are expected to appear on the CH(013) pole figure due to their very similar Bragg angles of 2θ=28.12° and 29.26°. However, they are not found in the same azimuth. Based on the latter argument, one can easily identify CH(112) and CH(013) reflections on Figure 2(b)(c).

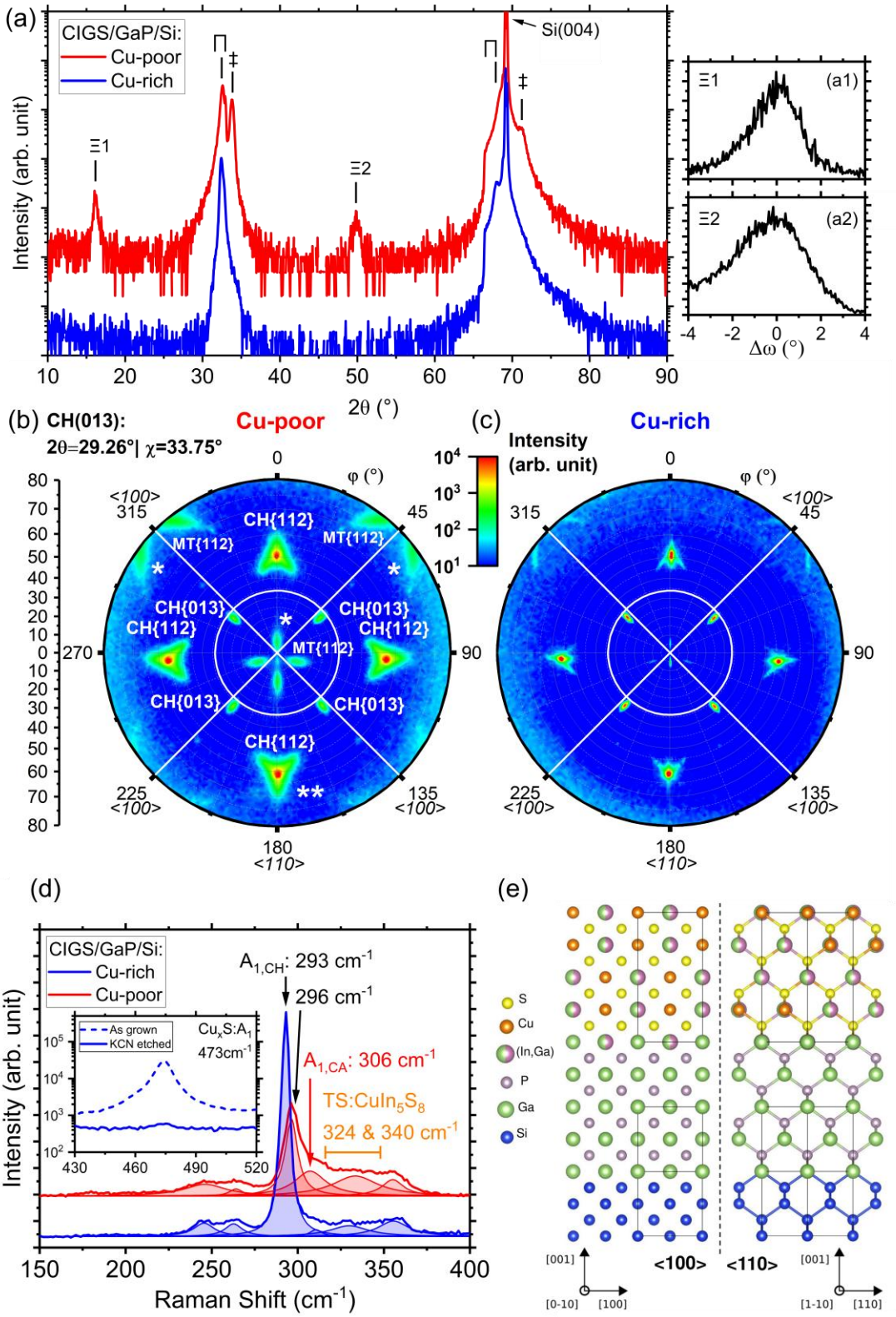

Figure 2: (a) Low resolution longitudinal ω/2ϑ scan along the [001] direction of the Si substrate. Transverse ω scans displaying the highly textures nature of the (a1) Ξ1 and (a2) Ξ2 CA peaks. (bc) Pole figures of the (b) Cu-poor and (c) Cu-rich sample at the theoretical Bragg angle of the CH(013) reflection, exclusive to the CH. A white crosshair point at the predicted position of the CH(013) planes, not accounting for the 6° miscut tilt. (d) Raman spectra of the Cu-rich and Cu-poor samples at 514nm excitation wavelength. Fitted peaks using Lorentzian function are drawn as a guide for the eye, and do not necessarily correspond to a specific or unique phonon mode. Inset: Zoom at the position of the

$Cu_{2-x}S$ A_1 peak for the as grown and KCN-etched Cu-rich sample. (e) Schematics of the crystal stack [41] corresponding to the following epitaxial relationship: CH[100](001)//GaP[100](001)//Si[100](001).

Interestingly, the rather weak CH(013) reflections are exclusive to the CH and stems from the original ordering of the CH cationic sublattice. Studying exclusive CH(013) reflections allows us to get a direct insight on the CH-ordered crystallites, minimizing misinterpretations due to crystals with similar symmetries. In Figure 2(b)(c), the presence of CH(013) reflections is a strong evidence that a high diffracting volume adopts the CH ordering, regardless of samples Cu content. For a crystal with a GGI of 0.2, the *c*-growth CH variant is expected the display CH-exclusive peaks in the <100> azimuthal directions at $\chi = 33.7°$ as indicated on Figure 2(b)(c) by a white crosshair. Contrarily, an a-growth variant would be revealed by signal in the same azimuth but at tilt angles of $\chi = 90 - 33.75 = 56.3°$ [18]. Therefore, Figure 2(b) and (c) demonstrate that for both samples, the *c*-growth variant is the natural growth variant of epi-CH on GaP/Si(001), without sign of the *a*-growth variant. To strengthen that analysis, a similar pole figure has been performed at the theoretical 2θ angle of a second CH-exclusive reflection, namely the CH(015). The data and its interpretation are presented in Figure S5. In a nutshell, the CH(015) planes exclusive to CH c-growth crystals are indeed visible on the pole figures of both samples. Therefore, we demonstrated that the most intense reflections present in both Cu-rich and Cu-poor samples on the survey scan in Figure 2(a) can be ascribed to the c-growth main CH phase sharing the following epitaxial relationship with the substrate: CH[100](001)//GaP[100](001)//Si[100](001). This means that the CH and the pseudo-substrate share the orientation sketched on Figure 2(e). We can retroactively update the indexation of the main CH reflections of Figure 2(a) as being multiples of the CH(00λ) plane family.

In summary, thorough XRD and Raman characterisation of the strongest ∏ reflections of Figure 2(a) reveal that can be ascribed to the main CH phase, in both samples. We determined that the CH tetragonal lattice grows with its *c*-axis orthogonal to the Si(001) plane exclusively.

5.4 Evaluation of defects and strain in the epitaxial CH-Cu(In,Ga)S_2 crystal

To study the strain and tilt state of the Cu-poor and Cu-rich overlayers, further investigation by mean of XRD reciprocal space mapping (RSM) is presented in Figure 3(a)(b), where the 2D detector is used to map the GaP and CIGS reflections around the Si(004) peaks. The diffraction signal is represented in reciprocal space in reduced scattering coordinate (S_x,S_z), with S_x contained in-plane and S_z orthogonal to the surface. CH(008) and weak GaP(004) nodes are found in the vicinity of the Si(004) substrate peak. It reveals that the scans of Figure 2(a) along Si[001] (i.e. along the full relaxation line) do not cut through the maximum of the CH reflections, for both samples; it follows that longitudinal ω /2θ scans presented in this work do not properly integrate the full extent of the CH reflections, artificially lowering their intensity. Indeed, the CH(008) is found to the left of the full relaxation line, rather than in-between the full relaxation and strain lines. This peculiar position in reciprocal space can be explained by a tilt exceeding 0.5° of the CH *c*-axis towards S_z, in addition to the full relaxation. This type of tilt has already been observed in $GaP_{1-x}Sb_x$/Si(001) heterostructures,

and is interpreted as the contribution of the miscut angle on the plastic relaxation [55]. Furthermore, the broadening of CH(008) reflections in the S_x in-plane directions indicate a rather high degree of micromosaic distribution (in accordance with ref. [56]) and/or poor in-plane correlation length.

Differences in peak width between the two samples can be spotted on Figure 3(a)(b). One can clearly see that the Cu-rich sample displays much more intense CH(004) peaks, one order of magnitude above the Cu-poor CH(004) intensity. Line profiles extracted from 2D RSM of Figure 3(a)(b) are displayed in Figure 3(c). Profiles are at set at $S_x = 0.6875 nm^{-1}$, integrated left and right over $\Delta S_x = \pm 0.005 nm^{-1}$, and fitted with pseudo-Voigt functions. The integral breadth β of the Cu-rich and Cu-poor are found to be $53.10^{-3} nm^{-1}$ and $108.10^{-3} nm^{-1}$, in the S_z direction. The sharpening of Cu-rich sample diffraction peaks is also apparent in Figure 2(a) and (b)(c) where CH(00λ) reflection and CH-exclusive CH(103) reflections respectively are found to be much sharper and more intense in the Cu-rich sample. Sharper peaks in the direction S_z can be related to a higher correlation length and compositional homogeneity along the growth direction.

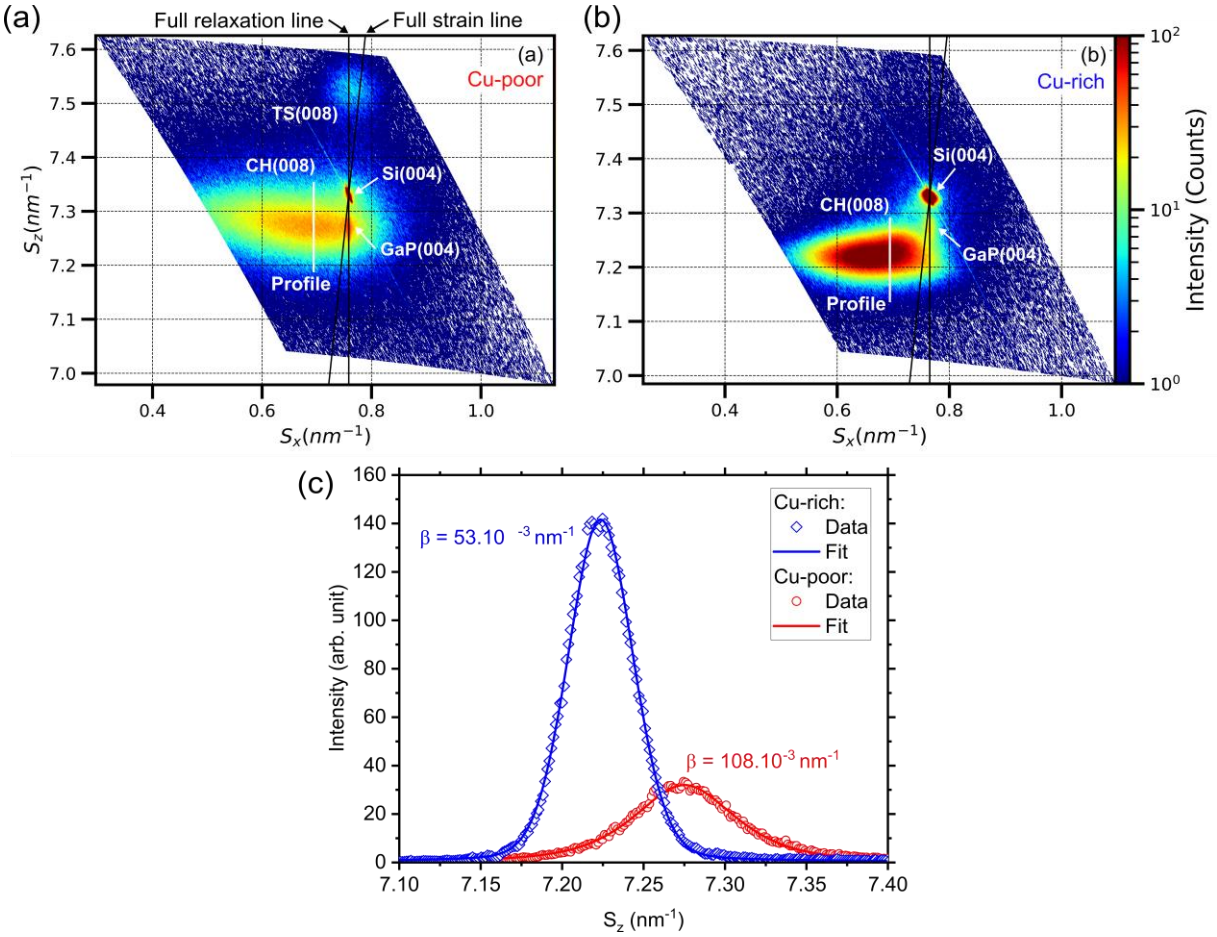

Figure 3: Reciprocal space maps of (a) the Cu-poor and (b) the Cu-rich sample around the Si(004) reflection, on the same logarithmic intensity scale. Full relaxation and full strain lines are drawn. The diffraction signal is represented in reciprocal space in reduced scattering coordinate $(S_x,S_z)=(Q_x,S_z)/2\pi$, with S_x contained in-plane and S_z orthogonal to the surface. (c) Line profiles from 2D maps, along S_z extracted at $S_x = 0.6875 \pm 0.0050 nm^{-1}$. Integral breadths β are extracted with pseudo-Voigt fits.

The sharpening of the Cu-rich sample diffraction peaks can be correlated to the lower microtwin defect density. Indeed, elongated reflections found in Figure 2(a)(b), close to the edges and to the centre of the pole figure, are ascribed to twin crystals (already observed in epi-CIGS/Si [18] and epi-CIGSe/GaP/Si [35]). More accurately, the elongation of reflections associated with twinning is the fingerprint of microtwins (MTs) domains, by analogy to GaP/Si on which similar observations were made [54]. Indeed, in the tetragonal CH system, twin boundaries running on the CH{112} planes marked with the symbol ** in Figure 2(b) create three additional elongated CH{112}-type planes marked by * and labelled MT{112}. Twinning displaces the CH{112} planes from the southern hemisphere to the northern hemisphere. The most central MT reflections is found at about 16° with respect to the Si(001) plane. An additional twinning across the same CH(112) planes reverts the crystal back to its original orientation. Thus, MTs can be described as the succession of two twin boundaries, separated by a few atomic planes, creating a narrow twin domain propagating along the twinning planes.CH(112) and MT(112) are expected to appear on the CH(013) pole figure due to their very similar Bragg angles of 28.12° and 29.26°. Therefore, the CH(112) and CH(013) pole figures in Figure S5(a)(b) and Figure 2(b)(c) respectively are very similar, and MT(112) are more apparent in Figure S5(a)(b). In total, 12 MT{112} reflections are visible in Figure 2(b)(c). Since each twin crystal creates three new MT{112} reflection each, a total of four twin variants are found in the epi-CIGS, in accordance with literature [18]. The lower intensity of peaks associated with MT(112) in the Cu-rich sample is consistent with a lower density of 2D MT defects, as compared to the Cu-poor sample.

In summary, the fully relaxed CH crystals of both samples exhibit a high degree of mosaicity or poor in-plane correlation length. A tilt of the *c*-axis is estimated to be 0.5° towards the surface normal. We evidenced four kinds of CH-MTs. The density of MTs is found to decrease in the Cu-rich sample, in comparison to the Cu-poor sample. This correlates to much sharper diffraction peaks in the Cu-rich samples than in Cu-poor sample, compatible with an overall higher correlation length of diffraction planes in the former. So far, only the most intense reflections labelled ⨅, shared by the two samples, have been dealt with.

5.5 Evaluation of secondary phases presence in Cu-poor epi-CIGS

It seems clear that weak intensity and short correlation lengths in the Cu-poor sample can be related to a higher MT density. However, another feature that needs to be addressed are the weak Ξ reflections at 2θ = 16.1° and 50.0° in Figure 2(a), and moderately intense contributions ‡ at 2θ = 33.8° and 71.2°, exclusively seen in the Cu-poor sample. In the following, we identify the origin of these two sets of peaks, in the light of candidate secondary phases, starting with the ‡ reflections.

One can notice in Figure 2(a) the presence of additional peaks marked ‡ found exclusively in the Cu-poor sample. These reflections can be more easily seen in Figure 4(a), where a high resolution XRD scan around the GaP(002) and GaP(004) reflections is displayed. We detect the intense ⨅ reflections ascribed to the CH, and the two moderately intense ‡ reflections at angles of 2θ = 33.8° and 71.2°. Based on the variation of *c* with the GGI (**Erreur ! Source du renvoi introuvable.** S6), the ‡ reflection could be wrongly interpreted as a signature of a fully relaxed CH crystal with a GGI of about 0.8; which is inconsistent with the Ga content

measured by EDX. A more convincing explanation would be the presence of a $CuIn_5S_8$ TS secondary phase, which would allow the indexation of the ‡ peaks at 2θ=33.8° and 71.2° as TS(00λ) peaks, somehow shifted relative to the theoretical position of $2\theta_{theo}$ = 33.55° and 70.44°. To further investigate the nature of the TS texture, reciprocal space is mapped around the position of Si(004) substrate peak and displayed in Figure 3(a). The TS(004) appears as a reflection at high diffraction vector S_z, ruling out the polycrystalline nature of the TS. To discriminate between fiber texture and epitaxy, and confirm the presence of the TS phase, we use the same strategy as in Section 5.3, which consists in studying the TS-exclusive reflection of the TS(022)=$TS(012)_{CH}$ plane family.

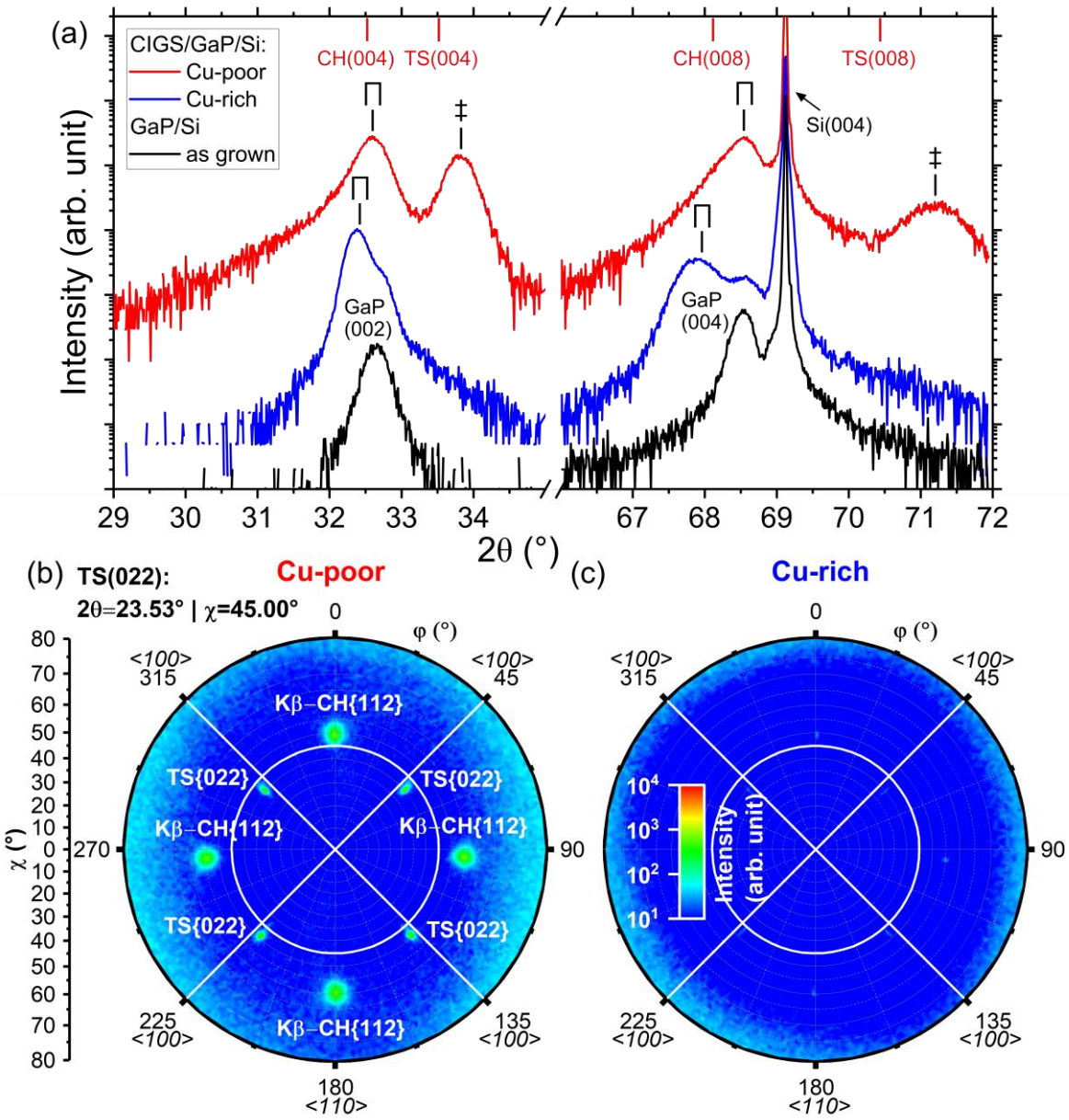

Figure 4: High-resolution scans of the Cu-poor and Cu-rich CIGS/GaP/Si stacks and of the GaP/Si platform alone, along the Si[001] displaying planes of the (00l) planar family. Theoretical angular positions of CH-$CuIn_{0.8}Ga_{0.2}S_2$ (2ϑ = 32.52° and 68.11°), and the TS phase (2ϑ = 33.52° and 70.44°) are given for reference. (bc) Pole figures of the (b) Cu-poor and (c) Cu-rich sample at the theoretical

Bragg angle of the TS(022)=TS(012)$_{CH}$ reflection, exclusive to the TS. A white crosshair point at the predicted position of the TS(022) planes, not accounting for the 6° miscut tilt.

On the pole figure displayed in Figure 4(b), one can see eight reflections for the Cu-poor sample. Four of them are found at the theoretical tilt χ and in the <110> azimuth of the CH(112) planes. These reflections are ascribed to an artifact originating from the scattering of Cu kβ X-rays by CH(112) planes (see Figure S3 for more details). The four other reflections match the expected tilt χ and <100> azimuth, indicated by a white circle, for the exclusive TS(022) reflections, demonstrating the presence of the TS phase. Furthermore, the TS(022) nodes are found exclusively in the <100> direction of the substrate, meaning that the $CuIn_5S_8$ TS shares an epitaxial relationship with the CH, and a fortiori with the GaP/Si(001) pseudo-substrate: TS[100](001)//CH[100](001). The sketches of Table 1 are chosen to reflect the orientation relation of the two phases.

Overall, the relative intensity of the ‡ TS(00λ) and ∏ CH(00λ) in Figure 4(a) suggests that a non-negligible fraction of the Cu-poor film adopts the TS structure, which is thermodynamically expected for such a deviation from stoichiometry (CGI=0.70 as determined by EDX). Figure 4(c) shows that the TS phase fingerprint disappears for the Cu-rich sample, in accordance with the fact that the Cu-rich sample is single-phase CH.

In Figure 4(a), the slight shift in 2θ of the TS phase relative to the theoretical position could be ascribed to the presence of Ga in the TS $CuIn_5S_8$. However, the literature suggests that the TS is unable to dilute large quantities of Ga, unlike the CH main phase [36]. In the light of the epitaxial nature of TS, the shifted position of the TS phase could be understood as strain. Indeed, about 2.6% lattice mismatch is expected between the TS and the CH assuming a GGI=0.2, which could lead to in-plane tensile strain. In turn, out-of-plane compressive strain would tend to shift the TS peak towards higher angles.

In the light of the presence of the TS phase is the Cu-poor sample a finer characterization of the main CH peak positions using high resolution XRD, can be initiated. High-resolution longitudinal scans of the CIGS/GaP/Si Cu-rich and Cu-poor samples, alongside the GaP/Si pseudo substrate alone, are displayed in Figure 4(a). The intense ∏ $(00\lambda)_{CH}$ peaks related to the CH phase are found at 2θ = 32.6° and 68.5° for the Cu-poor sample and 2θ = 32.4° and 67.9° for the Cu-rich sample. These important discrepancies in CH *c* lattice parameters between the Cu-rich (*c* =11.03Å) and the Cu-poor sample (*c* =10.95Å), can be explained by important differences in the GGI of the CH from one sample to the other. Indeed, a higher GGI in the Cu-poor sample's CH crystal, would decrease the lattice constant *c* of the CH phase. Indeed, assuming full relaxation of the CH crystals and knowing the evolution of *c* with the GGI (Figure S6), the CH in the Cu-rich sample is estimated to have a GGI = 0.15 while in the Cu-poor sample, the CH displays a GGI = 0.29. This analysis is backed up by the fits of the Raman spectra of Figure 2(b). The A_1 mode of the CH is found at 293cm^{-1} and 296cm^{-1} for the Cu-rich and Cu-poor sample respectively. Based on the linear dependence of the peak position with GGI [52], this can be interpreted as CH crystal with a GGI of about 0.10 and 0.25 Cu-rich and Cu-poor sample respectively. For the Cu-rich sample, good agreement between the GGI deduced from XRD (0.15), Raman (0.10) and measured by EDX (0.14) is obtained. However, for the Cu-poor sample, the GGIs deduced by XRD (0.29) and Raman

(0.25) are very different from the composition measured EDX (0.16). These discrepancies can be explained with the help of an observation made on polycrystalline CIGS films [53]. The TS is not able to accommodate large quantities of Ga in its structure [36]. As the CH and TS coexist in the Cu-poor film, most of the Ga is accommodated by the CH, so that the composition of the TS remains $CuIn_5S_8$. This boosts the GGI of the CH, even though the overall composition of the film remain unchanged. Since the TS phase tends to be located on the front side of the film [53], the TS containing Cu-poor sample most likely have a strong Ga gradient along the growth direction. On the contrary, in the monophasic Cu-rich sample, the Ga is most likely distributed in a more even manner in the CH, not excluding a soft GGI gradient along the growth direction.

In order to confirm the presence of the TS, Raman spectroscopy analyses have been performed. As shown in Figure 2(d), Raman spectra are recorded for the Cu-rich and Cu-poor sample. Qualitatively, the two spectra are different, namely in regard to the position of the main peak, and to the intensity of the signal in the range 305–370cm^{-1}. We have stated earlier that the spectrum of the Cu-rich sample is compatible with single-phase CH. This statement is untrue for the Cu-poor samples, for which we know that at least two sets of peaks cannot be explained by the CH phase alone, namely the ‡ TS(00λ) peaks and the Ξ peaks, unidentified so far. As a rule of thumbs, signal at Raman shifts above the main CH A_1 peak are typically ascribed to Cu-poor secondary phases, and the deconvolution is not straightforward [37]. $CuIn_5S_8$ has been demonstrated to give off a broad Raman signature in the range 320–340cm^{-1} [37]. In Figure 2(d), the increase in the Raman signal at 320–340cm^{-1} for the Cu-poor sample relative to the Cu-rich sample, is consistent with the segregation of TS evidenced by XRD. Finally, for the Cu-poor spectrum, we cannot rule out the presence of an additional mode, at 305–307cm^{-1} which may be ascribed to the A_1 mode of the CA phase [37].

In Figure 2(a), an obvious feature of the Cu-poor sample is the presence of additional reflections at 2θ = 16.1° and 50.0° marked with the symbol Ξ. These peaks are found at the 2θ of $(002)_{CH}$ and $(006)_{CH}$-type reflections, forbidden for the CH crystal structure. The highly textured nature of Ξ peaks is demonstrated by the transverse scans in Figure 2(a1)(a2). This suggest that the presence of a highly textured parasitic phase leads to a symmetry breaking in the Si[001] direction Assuming rational position for S atoms, the structure factor of the TS phase TS(00λ) planes, with λ = 2N + 2, N ∈ $\mathbb{N}_0$, can be approximated by $F_{00l} = 4(f_{Cu} - f_{In})(2y - 1)$, with y the occupancy ratio of Cu relative to In, in 4a sites. F_{00l} is non zero when $y \neq 0.5$. A special case arises when y = 0.5, for which the discussed symmetry is restored and TS(002)/TS(006) reflections are forbidden. In general, the TS symmetry does not forbid such $(002)_{CH}$ and $(006)_{CH}$-type reflections. Competing values of y = 0.296 [36] and y = 0.524 [57] have been reported, which may be due to different synthesis methods. As we have demonstrated that a non-negligible quantity of TS is present in the Cu-poor sample, one can think that TS may play a role in the presence of Ξ reflections.

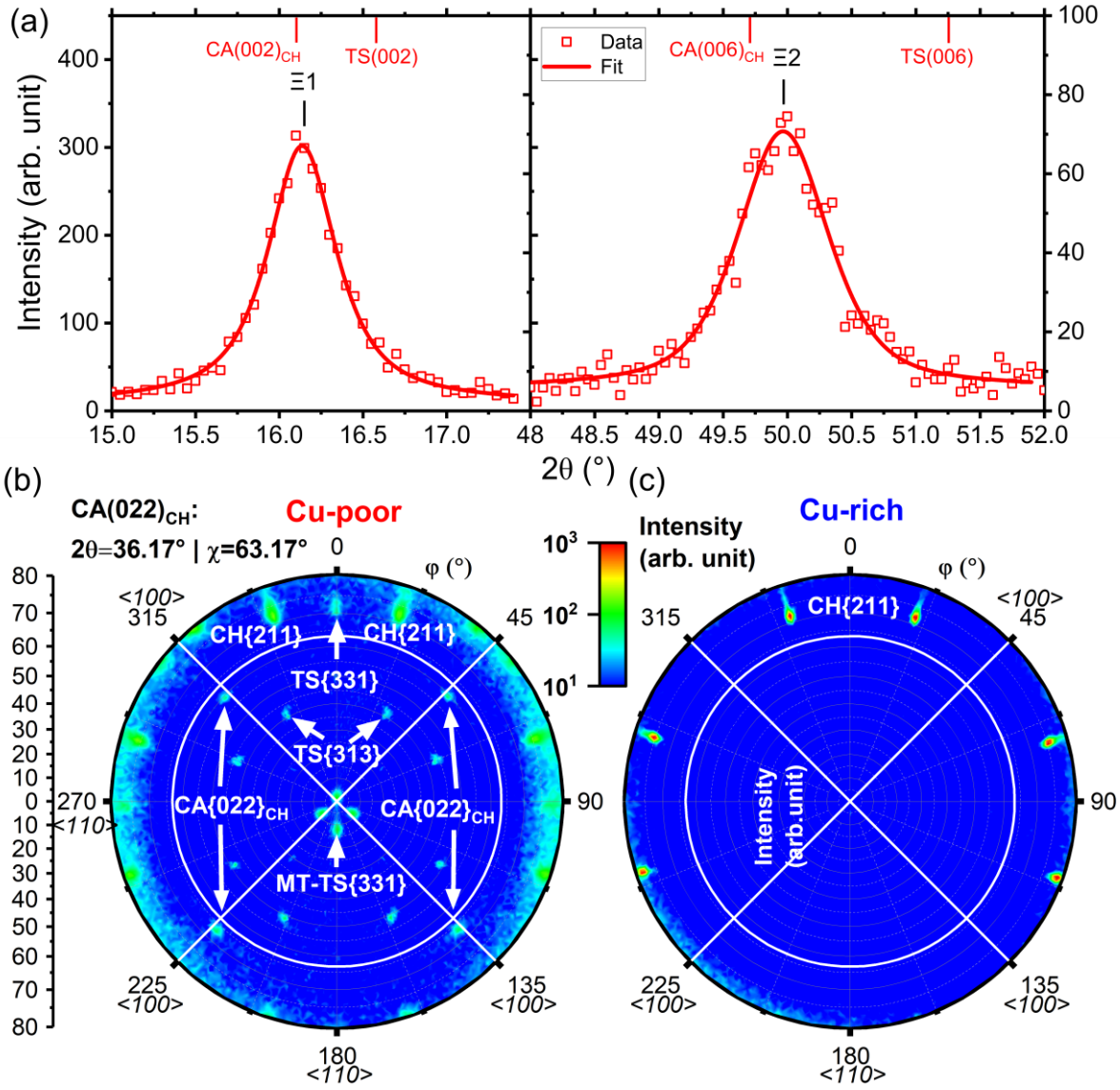

Figure 5: (a) Low-resolution scans around the CA(002)$_{CH}$ Ξ1 and CA(006)$_{CH}$ Ξ2 reflections, together with an asymmetric Kα$_1$ + Kα$_2$ pseudo-Voight fit. Theoretical positions of the CA(002)$_{CH}$ and CA(006)$_{CH}$ (2ϑ = 16.11° and 49.71°) and of the TS(002) and TS(006) (2ϑ = 16.58° and 51.25°) planes (bc) Pole figures of the (b) Cu-poor and (c) Cu-rich sample at the theoretical Bragg angle of the CA(111)=CA(022)$_{CH}$ reflection, exclusive to the CA. A white crosshair point at the predicted position of the CA(022)$_{CH}$ planes, not accounting for the 6° miscut tilt.

However, the Figure 5(a), which displays a low resolution scan of the weak (002)$_{CH}$/(006)$_{CH}$-type reflections. Indeed, taking a closer look at the Bragg angles of 2θ=16.13° and 49.96° for the latter reflections in Figure 5(a), better match is found with the theoretical 2θ position of (002)$_{CH}$/(006)$_{CH}$ planes of the CuAu-ordered phase, typically observed in epi-CIS/Si [19], rather than the TS phase. CA(002)$_{CH}$ and CA(006)$_{CH}$ reflections originate from the special ordering of planes composed of In atoms or of Cu atoms exclusively, as sketched in Table 1. Assuming rational reduced coordinates for S atom, the structure factor of the CuAu phase for CA(00λ)$_{CH}$ planes, with λ = 2N + 2, N ∈ $\mathbb{N}_0$, can be approximated by $F_{00l} = 2(f_{Cu} - f_{In})$. In this scattering vector direction, the antiphase diffusion of In and Cu atoms allow CA-exclusive reflexions indexed at CA(002)$_{CH}$ and CA(006)$_{CH}$. A small shift of the measured

position could be due to strain, a small incorporation of Ga into CA-CIS or the presence Cu vacancies.

These peaks exhibit extremely small intensities of 3 orders of magnitudes bellow the intensity of the strong CH(004) peak at 2θ = 32.5°. This suggests that only a small volume of CA is present in the Cu-poor sample. We perform a rough estimation of CA- $CuInS_2$ peak intensities performed with VESTA Software [41] based on lattice parameter of ref. [42]. The presence of the $CA(002)_{CH}$ at 2θ=16.13° indicate that a $CA(004)_{CH}$ peak of approximatively the same intensity is expected at 2θ=32.59°. The weak $CA(004)_{CH}$ peak is expected very near the very intense $CH(004)_{CH}$ peak at 2θ = 32.5°. Thus, the weak $CA(004)_{CH}$ is eclipsed by the CH(004) peak and is therefore not visible. We conclude, that the CA phase very weakly contributes to the CH reflections labelled ∏. The weakness of the CA fingerprint is here the sign that only a small volume fraction of the film crystallised in the form of a CA crystal.

Figure 5(b)(c) shows the pole figure obtained by selecting the Bragg angle of the CA-exclusive reflection $CA(111)=CA(022)_{CH}$ for the Cu-rich and Cu-poor samples. Numerous reflections can be seen on this pole figure and the indexation is not straightforward. The detailed indexation process using STEREOPOLE [43] is given in supplementary information **Erreur ! Source du renvoi introuvable.**. In the Cu-poor sample, one can see that weak reflections are found at the expected tilt χ = 63.17° of the $CA(022)_{CH}$ planes. The $CA(022)_{CH}$ reflections are found in the four Si<100> azimuthal directions of the substrate, proving the CA phase grows epitaxially relative to the CH phase: CA[110](001)//CH[100](001). We recall that the sketches of Table 1 are chosen to reflect the orientation relation of the competing phases. Interestingly, in the Cu-rich sample the fingerprint Ξ of the CA phase on Figure 2 (a) and on Figure 5(c) is eliminated, showing the absence of the CA phase in the Cu-rich sample

In summary, we found out that the non-CH reflections of Figure 2(a), exclusively found in the Cu-poor sample, can be ascribed to the TS phase (reflections labeled ‡) and the CA phase (reflections labeled Ξ). Additionally, both share the same epitaxy relationship with the CH and pseudo-substrate: TS[100](001)//CA[100](001)//CH[100](001)//GaP[100](001)//Si[100](001). No signs of these secondary phases are detected in the Cu-rich samples after KCN etching, demonstrating that the latter is single-phase CH.

6 Discussion

We have shown that Cu-poor growth conditions favor the presence of the TS and the CA. In this section, we confront our findings to the conclusions of the literature on epi-CIGS, and to the predictions of the already established thermodynamics of the Cu-In-Ga-S system. We put a focus on discussing the reason for CA elimination with Cu-excess, by exposing thermodynamic and kinetic considerations.

The elimination of the TS phase with Cu-excess is straightforward. The TS phase is only expected in Cu-poor samples from a thermodynamic standpoint [36]. Interestingly, only few articles report the presence of the TS in epi-$Cu(In,Ga)S_2$ [27]; this may be related to the fact that typical epitaxy processes, like MBE or metalorganic vapour-phase epitaxy (MOVPE),

allow a good control of the stoichiometry. Our study clearly shows that grain boundaries between the CH and TS tend to be highly symmetric, following an epitaxial relationship.

However, an explanation for the presence of metastable CA-$CuInS_2$ in the Cu-poor sample, and not in the Cu-rich sample, is not as trivial and may need a discussion. Our observation of the stabilisation of CA with Cu-deficiency in our sample is compatible with an already reported increase in CA yield with decreasing Cu content [37,58], in polycrystals. It partly confirms the work of Larsen et al. [37] on polycrystalline films. They note that the CA is often present in epitaxial samples [19,37] but is not as easily evidenced in polycrystals. The reason could be that small volume fractions of CA, due to its natural epitaxial relationship with the CH phase, are easily evidenced by XRD is epi-CIGS films, simply because all crystallites share the same orientation. Raman on the other hand is a powerful tool for CIGS phase identification, but it is often complicated to discriminate peaks in the rather feature-rich Raman spectra of Cu-poor CIGS [37]. It is also possible that epitaxy somehow stabilizes the CA, due to the strain [37] from lattice mismatch or thermal expansion mismatch with the substrate. Strain may tip the energetic balance towards CA stabilization, which would lead to a higher volume fraction of CA in epitaxial samples. However, we have shown that both our Cu-rich and CA-containing Cu-poor samples are most likely relaxed. Furthermore, both the epitaxial samples are deposited at the same temperature on the same GaP/Si platform. Therefore, we exclude stress induced by thermal and lattice mismatch as a reason for differences in CA yield in the Cu-poor and Cu-rich sample.

However, as stated before, to the best of our knowledge, no study aimed at understanding the influence of the overall Cu content on the structural properties of epi-CIGS. As a starting point of that discussion, it is necessary to consider the influence of the GGI on CA thermodynamic stability. According to the literature, several phases are often detected besides CH in epi-CIGS. We identify two often encountered non-CH cationic ordering in epi-CIGS, the disordered ZB phase and the metastable CA phase [56]. In the case of pure-In ternary epi-CIS MBE-grown sample on (111)- and (001)-oriented Si, the CA and ZB phases tend to coexist with the ground-state CH [22,56]. On the other hand, pure-Ga ternary $CuGaS_2$ exclusively crystallizes in the CH phase [18,21]. This demonstrates that the GGI plays an important role in CA stability in MBE-grown CIGS films. A systematic study on quaternary CIGS conducted by Metzner et al. [38] concluded to the coexistence of CH and CA orderings within CIGS films with the CH structure prevailing for higher GGI. This was later confirmed by Cieslak et al. [21] who reported a single-phase CH-ordered film for GGI > 0.4 while CH and CA coexist for GGI < 0.4, in accordance with previous work on ternary epi-CIS and epi-CGS. The presence of CA may be understood theoretically by considering the formation energies of the mentioned phases. Su and Wei [59] calculated the formation energy difference of the CA with respect to the reference ground state CH for CIS (2 meV/atom), $CuInSe_2$ (2 meV/atom) and $CuGaSe_2$ (9 meV/atom). Therefore, the unknown value for $CuGaS_2$ is speculated to be similar to that of $CuGaSe_2$. Consequently, in CIS, there exists only a small formation energy difference between the CA and CH structures; this may lead to a high probability of the formation of the metastable CA phase in epi-layers, in accordance with ref. [37]. Adding Ga elevates the formation energy of the unwanted CA phase and stabilizes the CH.

Both the Cu-rich and the Cu-poor sample have GGI far below 0.4; therefore, one could argue that the slight GGI difference between the two samples is not expected to influence the thermodynamic stability of the CA; the Cu content would be the decisive factor. However, this explanation would neglect the presence of strong local variation in GGI in the Cu-poor sample as a result of phase segregation of In-rich TS-$CuIn_5S_8$ and Ga-rich CH-$Cu(In,Ga)S_2$. Indeed, CA may find a stable environment in the most Ga-depleted part of the film, namely in the region near, or even within, the TS-$CuIn_5S_8$ inclusions. This would lead to an apparent correlation of the CA yield and the TS volume fraction, the latter naturally being causally linked to Cu-deficiency [36]. It follows that the absence of TS in the Cu-rich sample, and the overall homogeneous distribution of the Ga in the Cu-rich sample prevent the nucleation of In-rich regions, leading to the complete annihilation of the CA phase in Cu-excess conditions. Therefore, we speculate that one of the reasons for the presence of CA is of thermodynamic origin.

There exists only a small formation energy difference between the CA and CH structures; therefore, growth kinetics might be decisive for metastable CA yield. Indeed, no clear trend on the effect of Cu on CA yield can be extracted from the literature on epi-CIGS, since different growth techniques as well as different monocrystalline substrates, growth temperature, and film composition are used. Reports on epi-CIGS films grown in Cu-rich conditions exhibiting dominating CA phase exist [27]. This seemingly contradicts the fact that, from a thermodynamically standpoint, Cu-rich CIGS should be composed of stoichiometric CH alongside $Cu_{2-x}S$ [36]. However, in this reference [27], the film was grown at 200°C, and subsequently annealed at 400°C, much lower than the growth temperature of 570°C used in this our work. Some reports of stoichiometric epi-CIS/Si [56] conclude to the complete absence of CH in favor of a CA/ZB mixture, despite the substrate temperature of 570°C. In many articles, the CA phase is found to be the dominant ordering [27] in epi-CIGS with low Ga content, with up to 37% or even 80% in volume, according to ref. [21] and [56]. Furthermore, to the best of our knowledge, no single-phase CH film with GGI<0.4 is reported in the literature [21]. In our samples, even though the CA phase is present in our Cu-poor sample, the CA fingerprint is very weak. Furthermore, our Cu-rich epi-CIGS sample with a GGI < 0.2 is single-phase, and crystallizes as a CH. We concluded that the main crystal ordering is the CH in both samples.

These discrepancies between the CA yield of epi-CIGS reported in the literature and that of our epi-CIGS sample may be explained by the different deposition techniques employed. While we used coevaporation, typical epitaxial growth methods reported in the literature include MBE [21] and MOVPE [17]. To the best of our knowledge, examples of epitaxial growth of CIGS films using a coevaporation physical vapour deposition system, typically used for polycrystalline CIGS films, have not been reported. Thus, conclusions regarding the influence of the GGI on presence of CA were drawn from MBE-grown samples. These conclusions may not apply to coevaporated CIGS samples. Furthermore, disparate temperatures and compositions are explored [27,56], which surely altered the crystallisation kinetics of the growing films. Therefore, we argue that different growth rate and overall deposition kinetics may lead to different crystallisation modes, explaining the difference between our work and references cited so far. Indeed, lower temperature may result in an

increase in the metastable CA fraction. However, species mobility is not only dictated by temperature. It also depends on the CGI of the film. Indeed, in CIGSSe, fast recrystallization occurs as soon as the film turns Cu-rich (CGI>1) [5,60]. The CA being metastable [37,59], it is possible that the higher mobility of species in Cu-rich samples [5,60] allow the crystal to settle in the more stable CH structure. Contrarily, lower mobility of elements in Cu-poor CIGS [5] may freeze the crystal in a metastable CA structure.

To end the discussion, a limitation of our XRD-oriented study is the lack of conclusion on the presence or absence of metastable disordered ZB [37] which has been reported in epi-CIS [56]. The higher symmetry of the disordered-ZB means that it allows a lower number of reflections (which tend to coincide with the position of the main CH phase peaks). This prevents the study of ZB-exclusive reflections. Furthermore, Larsen et al. predicted that disordered ZB-CIGS can produce a Raman signature at 305cm^{-1}. Therefore, the attribution of the shoulder at 306cm^{-1} to CA in Figure 2(d) is not straightforward. We cannot exclude the presence of disordered ZB in our Cu-poor sample. In future work, electron diffraction using a transmission electron microscope would be a powerful tool to highlight and locate the ZB, as well as the CH, TS and CA, within the film, as their electron diffraction patterns would be easily distinguishable from each other.

7 Conclusions

KCN-etched Cu-rich and Cu-poor CIGS grown on GaP/Si(001) exhibit important structural differences. On the one hand, the Cu-poor CIGS film is found to be composed of at least three phases: the main Cu(In,Ga)S_2 CH phase, the In-rich $CuIn_5S_8$ TS phase and a small portion of metastable CA-CIS phase, all of which sharing an epitaxial relationship with each other and the GaP/Si(001) pseudo-substrate. On the other hand, the KCN-etched Cu-rich CIGS film is identified as a single-phase CH, and exhibits much shaper diffraction peaks. In both films, the main tetragonal CH crystal grows with its *c*-axis in the Si[001] out-of-plane direction, and coexists with 4 kinds of minor microtwins domains whose volume decreases in Cu-excess conditions. This study confirms previous works on the thermodynamics of the Cu-In-Ga-S system and the stability of secondary phases like the CA and $CuIn_5S_8$. We demonstrate that the CA phase can be eliminated if sufficient Cu-excess is provided during growth. This work paves the way to the future development of CIGS/Si tandem solar cells.

8 Acknowledgments:

This work is supported by the French National Research Agency project EPCIS (Grant no. ANR-20-CE05-0038). The authors are grateful to C. Derouet and V. Demange for their assistance on XRD measurements performed on Osirix platform (ScanMAT, UAR 2025 University of Rennes-CNRS. ScanMAT, received a financial support from the European Union through the European Regional Development Fund (ERDF), the Département d'Ille et Vilaine, Rennes Métropole and Région Bretagne (2015-2020 CPER project SCANMAT).

9 References

[1] M. Bär, W. Bohne, J. Röhrich, E. Strub, S. Lindner, M.C. Lux-Steiner, C.-H. Fischer, T.P. Niesen, F. Karg, Determination of the band gap depth profile of the penternary

Cu(In(1−X)GaX)(SYSe(1−Y))2 chalcopyrite from its composition gradient, Journal of Applied Physics. 96 (2004) 3857–3860. https://doi.org/10.1063/1.1786340.
[2] F. Martinho, Challenges for the future of tandem photovoltaics on the path to terawatt levels: a technology review, Energy Environ. Sci. 14 (2021) 3840–3871. https://doi.org/10.1039/D1EE00540E.
[3] T.P. White, N.N. Lal, K.R. Catchpole, Tandem Solar Cells Based on High-Efficiency c-Si Bottom Cells: Top Cell Requirements for >30% Efficiency, IEEE Journal of Photovoltaics. 4 (2014) 208–214. https://doi.org/10.1109/JPHOTOV.2013.2283342.
[4] O. Durand, E. Bertin, A. Létoublon, C. Cornet, N. Barreau, E. Gautron, A. Crossay, A. Rebai, D. Lincot, J. Lontchi, CIGS growth on a GaP/Si(001) platform: towards CIGS/Si tandem solar cells, in: Oxide-Based Materials and Devices XII, SPIE, 2021: p. 1168721. https://doi.org/10.1117/12.2591986.
[5] N. Barreau, E. Bertin, A. Crossay, O. Durand, L. Arzel, S. Harel, T. Lepetit, L. Assmann, E. Gautron, D. Lincot, Investigation of co-evaporated polycrystalline Cu(In,Ga)S2 thin film yielding 16.0 % efficiency solar cell, EPJ Photovolt. 13 (2022) 17. https://doi.org/10.1051/epjpv/2022014.
[6] S. Shukla, M. Sood, D. Adeleye, S. Peedle, G. Kusch, D. Dahliah, M. Melchiorre, G.-M. Rignanese, G. Hautier, R. Oliver, S. Siebentritt, Over 15% efficient wide-band-gap Cu(In,Ga)S2 solar cell: Suppressing bulk and interface recombination through composition engineering, Joule. 5 (2021) 1816–1831. https://doi.org/10.1016/j.joule.2021.05.004.
[7] S. Knack, Copper-related defects in silicon, Materials Science in Semiconductor Processing. 7 (2004) 125–141. https://doi.org/10.1016/j.mssp.2004.06.002.
[8] A.R. Jeong, S.B. Choi, W.M. Kim, J.-K. Park, J. Choi, I. Kim, J. Jeong, Electrical analysis of c-Si/CGSe monolithic tandem solar cells by using a cell-selective light absorption scheme, Scientific Reports. 7 (2017) 15723. https://doi.org/10.1038/s41598-017-15998-y.
[9] M. Raghuwanshi, E. Cadel, P. Pareige, S. Duguay, F. Couzinie-Devy, L. Arzel, N. Barreau, Influence of grain boundary modification on limited performance of wide bandgap Cu(In,Ga)Se2 solar cells, Appl. Phys. Lett. 105 (2014) 013902. https://doi.org/10.1063/1.4890001.
[10] T. Schwarz, A. Lomuscio, S. Siebentritt, B. Gault, On the chemistry of grain boundaries in CuInS2 films, Nano Energy. 76 (2020) 105081. https://doi.org/10.1016/j.nanoen.2020.105081.
[11] P. Jackson, R. Wuerz, D. Hariskos, E. Lotter, W. Witte, M. Powalla, Effects of heavy alkali elements in Cu(In,Ga)Se2 solar cells with efficiencies up to 22.6%, Physica Status Solidi (RRL) – Rapid Research Letters. 10 (2016) 583–586. https://doi.org/10.1002/pssr.201600199.
[12] S. Siebentritt, S. Sadewasser, M. Wimmer, C. Leendertz, T. Eisenbarth, M.Ch. Lux-Steiner, Evidence for a Neutral Grain-Boundary Barrier in Chalcopyrites, Phys. Rev. Lett. 97 (2006) 146601. https://doi.org/10.1103/PhysRevLett.97.146601.
[13] M.A. Contreras, L.M. Mansfield, B. Egaas, J. Li, M. Romero, R. Noufi, E. Rudiger-Voigt, W. Mannstadt, Wide bandgap Cu(In,Ga)Se 2solar cells with improved energy conversion efficiency: Wide bandgap Cu(In,Ga)Se2 solar cells, Prog. Photovolt: Res. Appl. 20 (2012) 843–850. https://doi.org/10.1002/pip.2244.
[14] J. Nishinaga, T. Nagai, T. Sugaya, H. Shibata, Shigeru Niki, Single-crystal Cu(In,Ga)Se2 solar cells grown on GaAs substrates, Appl. Phys. Express. 11 (2018) 082302. https://doi.org/10.7567/APEX.11.082302.

[15] H. Guthrey, A. Norman, J. Nishinaga, S. Niki, M. Al-Jassim, H. Shibata, Optical and Structural Properties of High-Efficiency Epitaxial Cu(In,Ga)Se $_2$ Grown on GaAs, ACS Appl. Mater. Interfaces. 12 (2020) 3150–3160. https://doi.org/10.1021/acsami.9b18040.

[16] D. Lincot, N. Barreau, A. Ben Slimane, T. Bidaud, S. Collin, M. Feifel, F. Dimroth, M. Balestrieri, D. Coutancier, S. Béchu, M. Bouttemy, A. Etcheberry, O. Durand, M.-A. Pinault-Thaury, F. Jomard, Exploring new convergences between PV technologies for high efficiency tandem solar cells : Wide band gap epitaxial CIGS top cells on silicon bottom cells with III-V intermediate layers, in: 35th European Photovoltaic Solar Energy Conference and Exhibition (EU PVSEC 2018), Bruxelles, Belgium, 2018: pp. 23–28. https://doi.org/10.4229/35thEUPVSEC20182018-1AO.2.2.

[17] M.S. Branch, P.R. Berndt, A.W.L. Leitch, J. Weber, J.R. Botha, An investigation into the ordering of metal atoms in CuGaS2 grown by MOVPE, Physica Status Solidi (a). 201 (2004) 2239–2244. https://doi.org/10.1002/pssa.200404835.

[18] K. Oishi, H. Katagiri, S. Kobayashi, N. Tsuboi, Growth of Cu(In,Ga)S2 on Si(100) substrates by multisource evaporation, Journal of Physics and Chemistry of Solids. 64 (2003) 1835–1838. https://doi.org/10.1016/S0022-3697(03)00107-0.

[19] Th. Hahn, H. Metzner, B. Plikat, M. Seibt, Order and disorder in epitaxially grown CuInS2, Thin Solid Films. 387 (2001) 83–85. https://doi.org/10.1016/S0040-6090(01)00790-8.

[20] S. Kobayashi, N. Tsuboi, T. Sega, K. Oishi, F. Kaneko, Growth of CuInS2 and CuIn5S8 on Si(001) by the Multisource Evaporation Method, Jpn. J. Appl. Phys. 42 (2003) 5485. https://doi.org/10.1143/JJAP.42.5485.

[21] J. Cieslak, Th. Hahn, H. Metzner, J. Eberhardt, W. Witthuhn, J. Kräußlich, F. Wunderlich, Epitaxial CuIn1−xGaxS2 on Si(111) $0 < x < 1$: Lattice match and metastability, PHYSICAL REVIEW B. (2020) 9.

[22] Th. Hahn, H. Metzner, J. Cieslak, J. Eberhardt, U. Reislöhner, J. Kräußlich, F. Wunderlich, S. Siebentritt, W. Witthuhn, Epitaxial Cu(In,Ga)S2 thin film solar cells, Journal of Physics and Chemistry of Solids. 66 (2005) 1899–1902. https://doi.org/10.1016/j.jpcs.2005.09.024.

[23] S. Chichibu, S. Shirakata, M. Uchida, Y. Harada, T. Wakiyama, S. Matsumoto, H. Higuchi, S. Isomura, Heteroepitaxial Growth of CuGaS 2 Layers by Low-Pressure Metalorganic Chemical Vapor Deposition, Jpn. J. Appl. Phys. 34 (1995) 3991. https://doi.org/10.1143/JJAP.34.3991.

[24] S. Shirakata, S. Chichibu, Photoluminescence of CuGaS2 epitaxial layers grown by metalorganic vapor phase epitaxy, Journal of Applied Physics. 87 (2000) 3793–3799. https://doi.org/10.1063/1.372416.

[25] R. Vequizo, S. Kobayashi, N. Tsuboi, K. Oishi, F. Kaneko, Epitaxial growth of CuInS2 thin films on (001)GaP by three-source evaporation, Physica Status Solidi c. 3 (2006) 2622–2625. https://doi.org/10.1002/pssc.200669658.

[26] R.M. Vequizo, S. Kobayashi, N. Tsuboi, K. Oishi, F. Kaneko, Ordering and Orientation of Epitaxial CuInS2 Films Grown on GaP(001) by Three-Source Evaporation, Jpn. J. Appl. Phys. 46 (2007) 716. https://doi.org/10.1143/JJAP.46.716.

[27] H. Metzner, T. Hahn, J.-H. Bremer, M. Seibt, B. Plikat, I. Dirnstorfer, B.K. Meyer, Structural and electronic properties of epitaxially grown CuInS2 films, Thin Solid Films. 361–362 (2000) 504–508. https://doi.org/10.1016/S0040-6090(99)00804-4.

[28] A. Crossay, D. Cammilleri, A. Thomere, B. Zerbo, A. Rebai, N. Barreau, D. Lincot, Elaboration of wide bandgap CIGS on silicon by electrodeposition of stacked metal

precursors and sulfur annealing for tandem solar cell applications, EPJ Photovolt. 11 (2019) 11. https://doi.org/10.1051/epjpv/2020008.
[29] Y. Takagi, Y. Furukawa, A. Wakahara, H. Kan, Lattice relaxation process and crystallographic tilt in GaP layers grown on misoriented Si(001) substrates by metalorganic vapor phase epitaxy, Journal of Applied Physics. 107 (2010) 063506. https://doi.org/10.1063/1.3310479.
[30] M.V. Lebedev, P.A. Dementev, T.V. Lvova, V.L. Berkovits, Modification of the p-GaP(001) work function by surface dipole bonds formed in sulfide solution, J. Mater. Chem. C. 7 (2019) 7327–7335. https://doi.org/10.1039/C9TC00210C.
[31] H. Emmer, C.T. Chen, R. Saive, D. Friedrich, Y. Horie, A. Arbabi, A. Faraon, H.A. Atwater, Fabrication of Single Crystal Gallium Phosphide Thin Films on Glass, Sci Rep. 7 (2017) 4643. https://doi.org/10.1038/s41598-017-05012-w.
[32] New Semiconductor Materials. Characteristics and Properties, (n.d.). http://www.ioffe.ru/SVA/ (accessed December 12, 2022).
[33] R. Hunger, C. Pettenkofer, R. Scheer, Surface properties of (111), (001), and (110)-oriented epitaxial CuInS2/Si films, Surface Science. 477 (2001) 76–93. https://doi.org/10.1016/S0039-6028(01)00707-5.
[34] M. Turcu, I.M. Kötschau, U. Rau, Composition dependence of defect energies and band alignments in the Cu(In1−xGax)(Se1−ySy)2 alloy system, Journal of Applied Physics. 91 (2002) 1391–1399. https://doi.org/10.1063/1.1432126.
[35] N. Barreau, O. Durand, E. Bertin, A. Létoublon, C. Cornet, P. Tsoulka, E. Gautron, D. Lincot, Epitaxial growth of CIGSe layers on GaP/Si(001) pseudo-substrate for tandem CIGSe/Si solar cells, Solar Energy Materials and Solar Cells. 233 (2021) 111385. https://doi.org/10.1016/j.solmat.2021.111385.
[36] A. Thomere, C. Guillot-Deudon, M. Caldes, R. Bodeux, N. Barreau, S. Jobic, A. Lafond, Chemical crystallographic investigation on Cu2S-In2S3-Ga2S3 ternary system, Thin Solid Films. 665 (2018) 46–50. https://doi.org/10.1016/j.tsf.2018.09.003.
[37] J.K. Larsen, K.V. Sopiha, C. Persson, C. Platzer-Björkman, M. Edoff, Experimental and Theoretical Study of Stable and Metastable Phases in Sputtered CuInS2, Advanced Science. 9 (2022) 2200848. https://doi.org/10.1002/advs.202200848.
[38] H. Metzner, J. Cieslak, J. Eberhardt, Th. Hahn, M. Müller, U. Kaiser, A. Chuvilin, U. Reislöhner, W. Witthuhn, R. Goldhahn, F. Hudert, J. Kräußlich, Epitaxial CuIn(1−x)GaxS2 on Si(111): A perfectly lattice-matched system for x≈0.5, Appl. Phys. Lett. 83 (2003) 1563–1565. https://doi.org/10.1063/1.1605239.
[39] Y. Ping Wang, J. Stodolna, M. Bahri, J. Kuyyalil, T. Nguyen Thanh, S. Almosni, R. Bernard, R. Tremblay, M. Da Silva, A. Létoublon, T. Rohel, K. Tavernier, L. Largeau, G. Patriarche, A. Le Corre, A. Ponchet, C. Magen, C. Cornet, O. Durand, Abrupt GaP/Si hetero-interface using bistepped Si buffer, Appl. Phys. Lett. 107 (2015) 191603. https://doi.org/10.1063/1.4935494.
[40] T. Quinci, J. Kuyyalil, T.N. Thanh, Y.P. Wang, S. Almosni, A. Létoublon, T. Rohel, K. Tavernier, N. Chevalier, O. Dehaese, N. Boudet, J.F. Bérar, S. Loualiche, J. Even, N. Bertru, A.L. Corre, O. Durand, C. Cornet, Defects limitation in epitaxial GaP on bistepped Si surface using UHVCVD–MBE growth cluster, Journal of Crystal Growth. 380 (2013) 157–162. https://doi.org/10.1016/j.jcrysgro.2013.05.022.
[41] K. Momma, F. Izumi, VESTA 3 for three-dimensional visualization of crystal, volumetric and morphology data, J Appl Cryst. 44 (2011) 1272–1276. https://doi.org/10.1107/S0021889811038970.

[42] D. Delmonte, F. Mezzadri, G. Spaggiari, S. Rampino, F. Pattini, D. Bersani, E. Gilioli, Metastable (CuAu-type) CuInS2 Phase: High-Pressure Synthesis and Structure Determination, Inorg. Chem. 59 (2020) 11670–11675. https://doi.org/10.1021/acs.inorgchem.0c01531.

[43] I. Salzmann, R. Resel, STEREOPOLE: software for the analysis of X-ray diffraction pole figures with IDL, J Appl Cryst. 37 (2004) 1029–1033. https://doi.org/10.1107/S002188980402165X.

[44] M.I. Alonso, K. Wakita, J. Pascual, M. Garriga, N. Yamamoto, Optical functions and electronic structure of CuInSe2 , CuGaSe2 , CuInS2 , and CuGaS2, Phys. Rev. B. 63 (2001) 075203. https://doi.org/10.1103/PhysRevB.63.075203.

[45] D. Drouin, A.R. Couture, D. Joly, X. Tastet, V. Aimez, R. Gauvin, CASINO V2.42—A Fast and Easy-to-use Modeling Tool for Scanning Electron Microscopy and Microanalysis Users, Scanning. 29 (2007) 92–101. https://doi.org/10.1002/sca.20000.

[46] CuInS2 Crystal Structure - SpringerMaterials, (n.d.). https://materials.springer.com/isp/crystallographic/docs/sd_0542570 (accessed September 6, 2022).

[47] Copper Gallium Sulfide, CuGaS2, (n.d.). https://www.matweb.com/search/datasheet.aspx?matguid=86d10c8fc25e43a3aec6b98be2677bf1&ckck=1 (accessed September 6, 2022).

[48] A. Elements, Gallium Phosphide, American Elements. (n.d.). https://www.americanelements.com/gallium-phosphide-12063-98-8 (accessed January 24, 2023).

[49] 2.3.1 Crystalline Silicon, (n.d.). https://www.iue.tuwien.ac.at/phd/hoessinger/node26.html (accessed January 24, 2023).

[50] L. Choubrac, E. Bertin, F. Pineau, L. Arzel, T. Lepetit, L. Assmann, T. Aloui, S. Harel, N. Barreau, On the role of sodium and copper off-stoichiometry in Cu(In,Ga)S 2 for photovoltaic applications: Insights from the Investigation of more than 500 samples, (2022). https://doi.org/10.22541/au.167180672.26971816/v1.

[51] A. Lafond, C. Guillot-Deudon, S. Harel, A. Mokrani, N. Barreau, S. Gall, J. Kessler, Structural study and electronic band structure investigations of the solid solution NaxCu1−xIn5S8 and its impact on the Cu(In,Ga)Se2/In2S3 interface of solar cells, Thin Solid Films. 515 (2007) 6020–6023. https://doi.org/10.1016/j.tsf.2006.12.044.

[52] S. Shukla, D. Adeleye, M. Sood, F. Ehre, A. Lomuscio, T.P. Weiss, D. Siopa, M. Melchiorre, S. Siebentritt, Carrier recombination mechanism and photovoltage deficit in 1.7-eV band gap near-stoichiometric Cu(In,Ga)S2, Phys. Rev. Materials. 5 (2021) 055403. https://doi.org/10.1103/PhysRevMaterials.5.055403.

[53] A. Thomere, N. Barreau, N. Stephant, C. Guillot-Deudon, E. Gautron, M.T. Caldes, A. Lafond, Formation of Cu(In,Ga)S2 chalcopyrite thin films following a 3-stage co-evaporation process, Solar Energy Materials and Solar Cells. 237 (2022) 111563. https://doi.org/10.1016/j.solmat.2021.111563.

[54] Y. Ping Wang, A. Letoublon, T. Nguyen Thanh, M. Bahri, L. Largeau, G. Patriarche, C. Cornet, N. Bertru, A. Le Corre, O. Durand, Quantitative evaluation of microtwins and antiphase defects in GaP/Si nanolayers for a III–V photonics platform on silicon using a laboratory X-ray diffraction setup, J Appl Cryst. 48 (2015) 702–710. https://doi.org/10.1107/S1600576715009954.

[55] M. Alqahtani, S. Sathasivam, L. Chen, P. Jurczak, R. Piron, C. Levallois, A. Létoublon, Y. Léger, S. Boyer-Richard, N. Bertru, J.-M. Jancu, C. Cornet, J. Wu, I.P. Parkin, Photoelectrochemical water oxidation of GaP1−xSbx with a direct band gap of 1.65 eV for full spectrum solar energy harvesting, Sustainable Energy Fuels. 3 (2019) 1720–1729. https://doi.org/10.1039/C9SE00113A.

[56] Th. Hahn, H. Metzner, B. Plikat, M. Seibt, Epitaxial growth of CuInS2 on sulphur terminated Si(001), Appl. Phys. Lett. 72 (1998) 2733–2735. https://doi.org/10.1063/1.121074.

[57] L. Gastaldi, L. Scaramuzza, On the space groups of two thiospinels, Acta Cryst B. 35 (1979) 2283–2284. https://doi.org/10.1107/S0567740879009092.

[58] E. Rudigier, I. Luck, R. Scheer, Quality assessment of CuInS2-based solar cells by Raman scattering, Appl. Phys. Lett. 82 (2003) 4370–4372. https://doi.org/10.1063/1.1582362.

[59] D.S. Su, S.-H. Wei, Transmission electron microscopy investigation and first-principles calculation of the phase stability in epitaxial CuInS2 and CuGaSe2 films, Appl. Phys. Lett. 74 (1999) 2483–2485. https://doi.org/10.1063/1.123014.

[60] N. Barreau, T. Painchaud, F. Couzinié-Devy, L. Arzel, J. Kessler, Recrystallization of CIGSe layers grown by three-step processes: A model based on grain boundary migration, Acta Materialia. 58 (2010) 5572–5577. https://doi.org/10.1016/j.actamat.2010.06.025.